ADVANCED FUNCTIONAL MATERIALS
www.afm-journal.de

In Situ Structure Modulation of Cathode-Electrolyte Interphase for High-Performance Potassium-Ion Battery

Fengchun Li, Xin Gu, Akang Cui, Yang Li, Sijin Dong, Shuang Wu, Zhenjie Cheng, Qian Yao, Jian Yang,* and Mingbo Wu**

Manganese-based layered oxide cathodes, particularly K_xMnO_2 (KMO), have shown great potential in potassium-ion batteries (PIBs) due to their low cost, high theoretical capacities, and excellent thermal stability. However, Jahn-Teller distortion, manganese dissolution, and interface instability of electrode/electrolyte lead to structural instability and performance decay. Here, lithium difluoro(oxalate) borate (LiDFOB) is introduced as an electrolyte additive to improve the electrochemical performance of P3-type KMO. LiDFOB creates a uniform, thin, and robust cathode-electrolyte interphase layer on the cathode surface, enhancing reaction kinetics, preventing manganese dissolution, and stabilizing the structure. The P3-KMO cathode with LiDFOB in the basic electrolyte exhibits significantly improved electrochemical performance, such as a remarkable Coulombic efficiency of ≈99.5% and high capacity retention of 78.6% after 300 cycles at 100 mA g^{-1}. Moreover, the full cell of P3-KMO||soft carbon demonstrates satisfactory specific capacity and energy density. This study emphasizes the importance of interface chemistry for PIBs.

1. Introduction

Efficient and affordable secondary batteries are garnering attention from both academia and industry due to their potential to meet the growing demand for consumer electronics and electric vehicles, as well as address the intermittency of renewable energy sources such as solar and wind power.[1–4] While lithium-ion batteries exhibit high energy/power density and long cycle life, their widespread use is hindered by uneven resource distribution and limited availability.[5–7] Potassium-ion batteries (PIBs) have significant potential for large-scale energy storage thanks to abundant potassium resources, low redox potential, and favorable intercalation chemistry in graphite.[8–10] Nevertheless, compared to the relatively successful research on anode hosts, the investigation of cathode hosts for PIBs is much more challenging due to the large radius of potassium ions.

Extensive research has led to the development of cathodes for PIBs, such as Prussian blue analogs (PBAs),[11,12] polyanionic compounds,[13] and layered metal oxides.[14,15] However, PBAs' high water content and polyanionic compounds' low specific capacity hinder their practical applications. On the other hand, manganese-based layered oxide cathodes, particularly K_xMnO_2 (KMO, 0<x<1), have gathered attention due to their cost-effectiveness, high theoretical capacities, and excellent thermal stability.[16–21] However, KMO cathodes are vulnerable to complex structural transformations, Jahn-Teller distortions, and Mn dissolution.[22–27] Additionally, insufficient cathode-electrolyte interphase (CEI) protection leads to continuous electrolyte decomposition and low Coulombic efficiency (CE < 95%), causing rapid capacity decay of KMO cathodes.

It has been noted that incorporating transition metals, like Cu, Mg, Ni, Co, Fe, or Ti, can assist in reducing Jahn-Teller distortion, enhancing specific capacity, and stabilizing KMO's structure.[19,28–36] A coating layer of amorphous $FePO_4$ was applied to $K_{0.5}Ni_{0.1}Mn_{0.9}O_2$ to ensure strain relaxation and fast K-conducting capability.[19,28–36] A report suggested that replacing ethylene carbonate/diethyl carbonate (EC/DEC) with nonflammable triethyl phosphonate (TEP) in the electrolyte can prevent EC intercalation and ensure stable electrochemical performance for P3-KMO.[37] Creating a stable CEI layer on the cathode surface can also effectively address the issues mentioned in PIBs. For instance, Lei et al. used 6.0 M potassium bis(fluoro sulfonyl)amide in diglyme as the electrolyte to develop a CEI layer and an inactive K-poor spinel interlayer on the P2-KMO surface. The dual interphase layers-modified P2-KMO cathode achieved a high capacity retention of 90.5% and a CE of ≈100% after 300 cycles.[38] However, the regulation of CEI on cathode is still a relatively new concept.

This work employs lithium difluoro(oxalate) borate (LiDFOB) as an electrolyte additive in PIBs for the first time, even though it has been previously used in conventional lithium batteries.[39–42] X-ray photoelectron spectroscopy (XPS) and time-of-flight secondary ion mass spectrometry (TOF-SIMS) demonstrate that

F. Li, X. Gu, A. Cui, Y. Li, S. Dong, S. Wu, M. Wu
College of New Energy, State Key Laboratory of Heavy Oil Processing
China University of Petroleum (East China)
Qingdao 266580, P. R. China
E-mail: guxin@upc.edu.cn; wumb@upc.edu.cn
Z. Cheng, Q. Yao, J. Yang
Key Laboratory of Colloid and Interface Chemistry, Ministry of Education,
School of Chemistry and Chemical Engineering
Shandong University
Jinan 250100, P. R. China
E-mail: yangjian@sdu.edu.cn

DOI: 10.1002/adfm.202313146

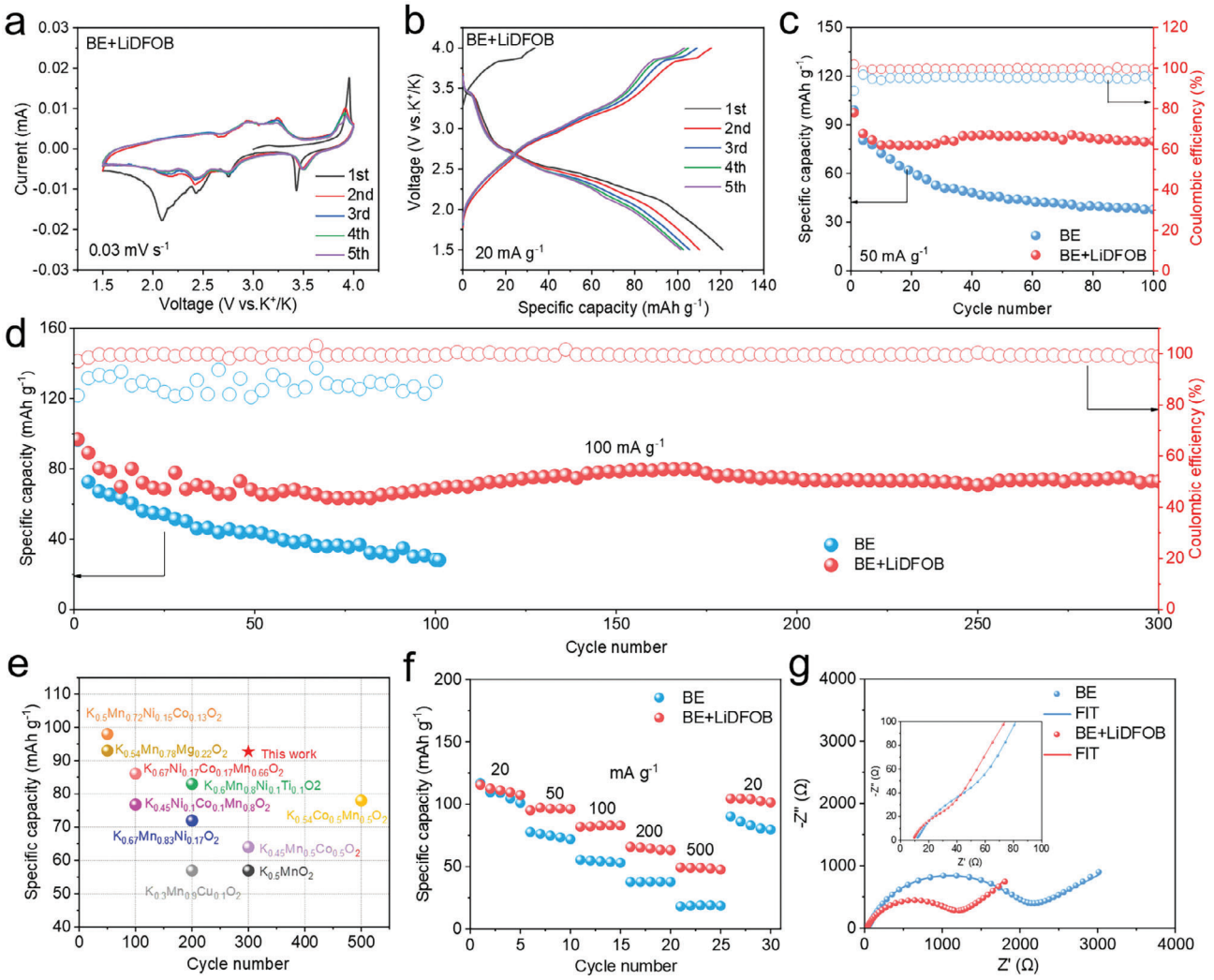

Figure 1. a) CV profiles at 0.03 mV s^{-1} and b) Charge/discharge profiles at 20 mA g^{-1} of K||KMO in BE+LiDFOB. c) Cycle performance and Coulombic efficiencies of K||KMO with different electrolytes at 50 mA g^{-1}. d) Long-range cycle performance and Coulombic efficiencies of K||KMO with different electrolytes at 100 mA g^{-1}. e) Comparison of the cycle performance with the reported data in PIBs. f) Rate performance of K||KMO with different electrolytes. g) Nyquist plots of K||KMO with different electrolytes after 30 cycles.

LiDFOB participates in the formation of CEI and effectively inhibits the decomposition of electrolyte solvents, resulting in a CEI layer enriched with F and B but containing fewer C and O species. The CEI layer is found to be uniform, thin, and robust, as confirmed by high-resolution transmission electron microscopy (HRTEM) and atomic force microscopy (AFM). This leads to enhanced reaction kinetics, stabilized crystal structure, and reduced manganese dissolution. The P3-KMO cathode with a F- and B-rich CEI layer exhibits a high capacity retention of 78.6% and a CE of ≈99.5% after 300 cycles at 100 mA g^{-1}, highlighting the promising potential of CEI layers on KMO cathode in PIBs.

2. Results and Discussion

Figure S1 (Supporting Information) shows the structure characterization of KMO. X-ray diffraction (XRD) patterns and Rietveld refinement infer that KMO is in a P3-type structure with a space group of *R3m*, as shown in Figure S1a (Supporting Information). This structure comprises oxygen atoms arranged in parallel layers in the order of ABBCCA, while Mn atoms occupy the octahedral sites and K atoms are located at the prismatic sites, as depicted in Figure S1b (Supporting Information). Figure S1c (Supporting Information) shows that KMO powders are granular with particle sizes in a range of 2–4 µm. Additionally, the inductively coupled plasma optical emission spectra (ICP-OES) reveal that the molar ratio of K-to-Mn is 0.49 (Figure S1d, Supporting Information).

The effects of LiDFOB as an electrolyte additive on the electrochemical performance of K||KMO are investigated. The cyclic voltammetry (CV) profiles of K||KMO using the modified electrolyte (BE+LiDFOB) are shown in **Figure 1**a. Four redox couples are observed at 2.56/2.15, 2.93/2.43, 3.24/2.75, and 3.92/3.50 V. The redox couple at 3.92/3.50 V is attributed to a phase transition, while the remaining three are associated with the

transformation of ordered/disordered K^+/vacancy and the gliding of the MO_2 layer during K-ion insertion/ extraction.[38,43,44] The subsequent scans of the CV profiles reveal that the KMO electrode in BE+LiDFOB has excellent reversibility. On the other hand, the CV profiles of the KMO electrode in the basic electrolyte (BE) (Figure S2, Supporting Information) display four pairs of redox peaks similar to those in BE+LiDFOB. This finding suggests that the additive does not alter the electrochemical reactions, and Li^+ does not participate in the electrochemical reactions. However, it is noted that the peaks with BE show a significant and continuous decay, indicating severe irreversible phase transitions and instability. The charge/discharge profiles of K||KMO in both electrolytes at 20 mA g^{-1} are depicted in Figure 1b and Figure S3 (Supporting Information), revealing different voltage platforms consistent with the CV results.

Figure 1c shows the cycle performance and CEs of K||KMO with and without LiDFOB in the electrolyte at 50 mA g^{-1}. Notably, the KMO electrode with BE+LiDFOB displays an unprecedented capacity retention of 91.1% compared to the second cycle and a CE of approximately 99.95% after 100 cycles. On the other hand, the specific capacity in the BE retains only 42.7% and shows a low CE of around 94.68%. The inferior CE implies severe parasitic reactions on the electrode, resulting in rapid capacity decay. The amount of LiDFOB additive in the electrolyte requires a balance between low salt solubility and consumption during cycling. To determine the optimum content of LiDFOB, we tested the electrochemical performance of K||KMO half cell with various contents of LiDFOB in the electrolyte (0, 0.2%, 0.5%, 0.7%, 1.5%), as shown in Figure S4 (Supporting Information). The optimal LiDFOB content for maintaining the cycle lifespan and cycling stability is 0.7%. However, if the LiDFOB content is increased beyond this data, it may become insoluble in the basic electrolyte (Figure S5, Supporting Information), reducing the electrochemical performance of the KMO electrode. Hence, the discussion about the effect of LiDFOB refers to 0.7% LiDFOB without special denotation. In addition to the cathode, LiDFOB could also influence the anode. To determine how LiDFOB affects the K electrode in K||KMO batteries, the plating and stripping behaviors of K were examined using symmetrical K||K cells. These cells were cycled at a current density of 0.02 mA cm^{-2} (Figure S6, Supporting Information). It is worth mentioning that the K||K symmetrical cell, when cycled in an electrolyte containing LiDFOB, displays a more significant degree of polarization compared to the basic electrolyte. It can be inferred that the performance improvement of the K||KMO half cell mainly comes from the cathode side. Figure 1d presents the long-term cycling performance of K||KMO in the presence and absence of LiDFOB at 100 mA g^{-1}. The cell fails after 100 cycles in BE, as the CE drops to only 89.1%, and the specific capacity decreases from 96.6 to 28.4 mAh g^{-1}. However, by adding LiDFOB, the CE stabilizes at ≈99.5%, and the specific capacity gradually decays to 72.9 mAh g^{-1} over 300 cycles, retaining a high capacity retention of 78.6% relative to the second cycle. The impressive CE in BE+LiDFOB indicates that the LiDFOB-induced CEI effectively suppresses electrolyte consumption and Mn dissolution, improving capacity retention. It is noticed that the specific capacity of KMO increases in BE+LiDFOB during cycles. To reveal the reasons for this increase in capacity, the differential capacity (dQ/dV) curves of KMO in BE+LiDFOB at the 30th and 150th cycle at 100 mA g^{-1} (Figure S7, Supporting Information). At the 30th cycle, the average polarization of the redox couples is 1.74 V. At the 150th cycle, the average polarization decreases to 1.53 V. The phenomenon may be due to the decomposition of LiDFOB generating special gases, such as CO_2, which leads to an increase in polarization and a decrease in capacity.[45,46] After dozens of cycles, LiDFOB is exhausted, contributing to decreased polarization and increased capacity. This phenomenon has been previously reported.[47,48] The cycle performance of KMO surpasses most previously reported results (Figure 1e).[16,28,30,31,49–54] Also, the rate performance was tested in both electrolytes (Figure 1f). KMO delivers the discharge capacities of 115.6, 95.1, 81.9, 65.8, and 49.3 mAh g^{-1} at the current densities of 20, 50, 100, 200, and 500 mA g^{-1}, respectively. As the current density comes back to 20 mA g^{-1}, the cathode recovers a reversible capacity of 104.5 mAh g^{-1}. However, the specific capacity in BE declines as the current density increases. Upon returning to 20 mA g^{-1}, KMO shows a discharge capacity of only 90.2 mAh g^{-1}, followed by persistent capacity decay. Figure S8 (Supporting Information) shows the voltage profiles of KMO in BE or in BE+LiDFOB at different current densities. We measured the electrochemical impedance spectra (EIS) of KMO in different electrolytes. The EIS spectra of KMO in BE or in BE+LiDFOB have the similar Nyquist plots (Figure 1g). These plots comprise a semicircle representing the CEI impedance (R_{CEI}) and the charge-transfer impedance (R_{ct}) at the electrode/electrolyte interface, as well as a straight line corresponding to the Warburg impedance (Z_w). By utilizing the equivalent circuit, we observed that both the R_{CEI} and R_{ct} decrease by the addition of LiDFOB (Table S1, Supporting Information). This decrease is due to a thinner CEI layer and less by-product formation, indicating an improvement in charge transfer dynamics. As shown in Figure S9 (Supporting Information), the slope of the line associated with the K^+ diffusion coefficient, known as the Warburg factor (σ), is derived from the low-frequency region. Therefore, KMO with LiDFOB shows an improved K^+ diffusion coefficient (D_{k+}) of 2.5×10^{-12} cm^2 s^{-1} compared to that without LiDFOB (2.3×10^{-12} cm^2 s^{-1}).

The CEI components on KMO after 100 cycles in different electrolytes were characterized by XPS coupled with Ar-ion sputtering. The survey spectra of KMO cycled in BE or in BE+LiDFOB reveal that both CEI layers retain the signals of C, O, P, F, and K elements (Figures S10 and S11, Supporting Information). The CEI layer in BE+LiDFOB presents the additional signals of Li 1s (56 eV) and B 1s (194 eV), which can be attributed to the decomposition of LiDFOB.[40] Figures 2a,b illustrate the variations of these elements at different depths in BE and BE+ LiDFOB. By adding LiDFOB additive to BE, the content of B species increases from zero to 4.5 at%, and that of F species increases from 6.7 to 24.6 at%, with a sputtering depth of 0 s. Conversely, the concentration of C species decreases from 54.7 to 47.4 at%, and that of O content drops from 25.8 to 13.4 at%. Moreover, the fluctuations in C, F, O, and B concentrations at sputtering depths of 50 and 100 s exhibit consistency with those observed at a depth of 0 s. These findings suggest LiDFOB-tuned CEI is rich in F and B species due to DFOB-ligand involvement during initial cycling. The decrease in C and O species indicates that the F- and B-rich CEI functions as a protective layer for the KMO cathode, effectively mitigating ongoing side reactions with the electrolyte.[55] High-resolution XPS spectra were detected to unveil the

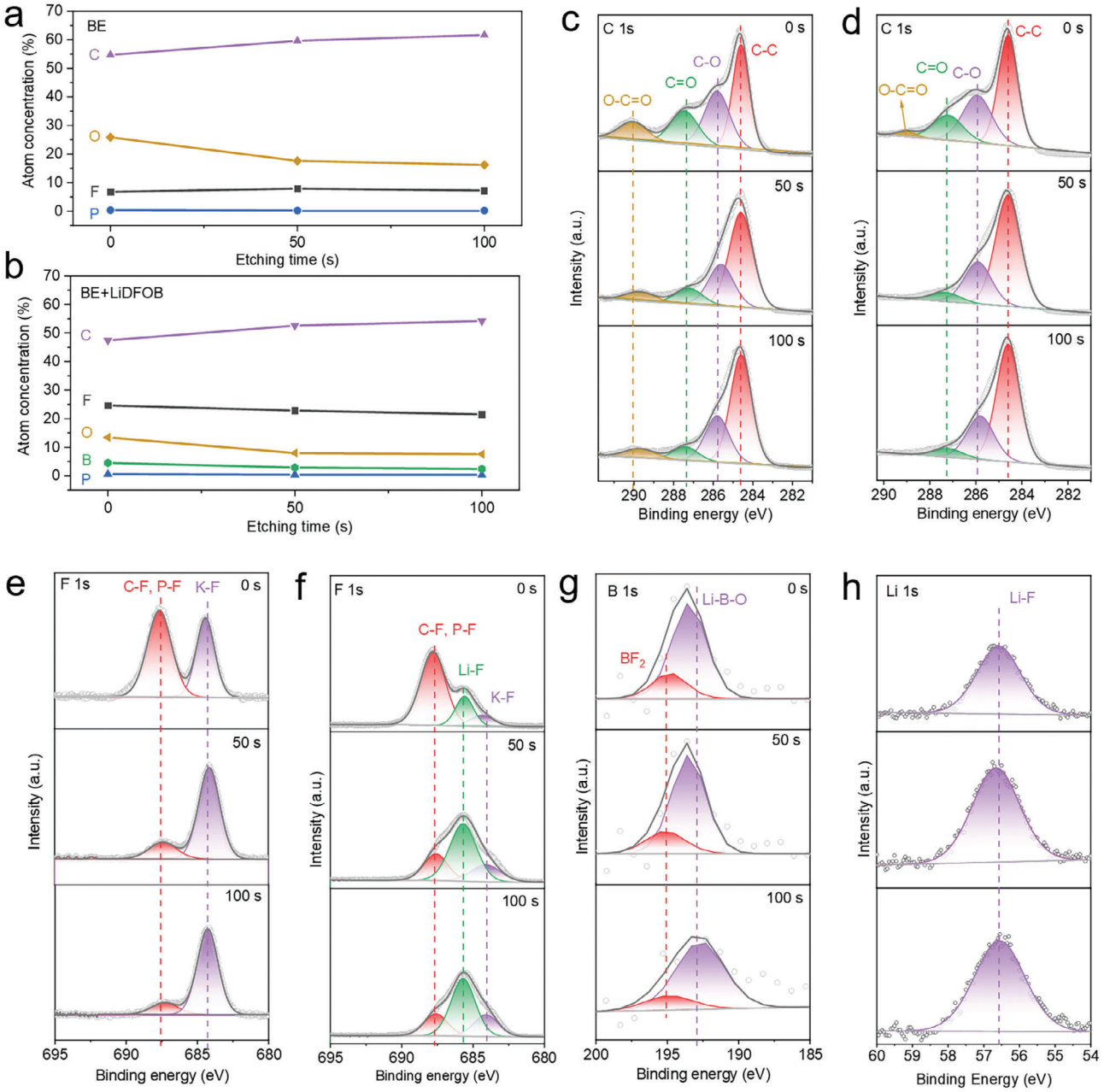

Figure 2. Characterization of the CEI components on KMO cathode after 100 cycles in different electrolytes by XPS. Atom concentration on the cycled KMO electrode with varied sputtering depth in a) BE and b) BE+LiDFOB. The XPS depth profiles of C 1s for the cycled KMO electrode in c) BE and d) BE+LiDFOB after sputtering for 0, 50, and 100 s. The XPS depth profiles of F 1s for the cycled KMO electrode in e) BE and f) BE+LiDFOB after sputtering for 0, 50, and 100 s. The XPS depth profiles of g) B 1s and h) Li 1s for the cycled KMO electrode in BE+LiDFOB after sputtering for 0, 50, and 100 s.

underlying insights of CEI. The peaks of C—O (286.5 eV), C═O (287.7 eV), and O—C═O (289.6 eV) arise from electrolyte decomposition (Figure 2c,d).[40] The CEI layer formed in BE+LiDFOB exhibits a decreased presence of C—O, C═O, and O—C═O compared to BE (Figure 2d; Figure S12, Supporting Information), signifying a reduced extent of solvent decomposition. Additionally, the decrease in the C═O content observed in the O 1s data (Figure S13a, Supporting Information) relative to BE (Figure S13b, Supporting Information) aligns with the findings in the C 1s data. The diminished contents of C—O and C═O in BE+LiDFOB can be attributed to the suppressed side reactions, significantly reducing surface resistance (Figure 1g). The XPS spectra of F 1s (Figure 2f) display a distinct signal of LiF (685.6 eV) in BE+LiDFOB, while it is almost invisible in the case of BE (Figure 2e). It confirms the significant presence of LiF in the CEI resulting from the LiDFOB additive.[56] Furthermore, the content of KF (684.3 eV) diminishes on the surface of KMO cycled in BE+LiDFOB compared to that in BE. The increasing content of LiF (high Young's modulus, 64.97 GPa) and the decreasing content of KF (low Young's modulus, 29 GPa) enhance the

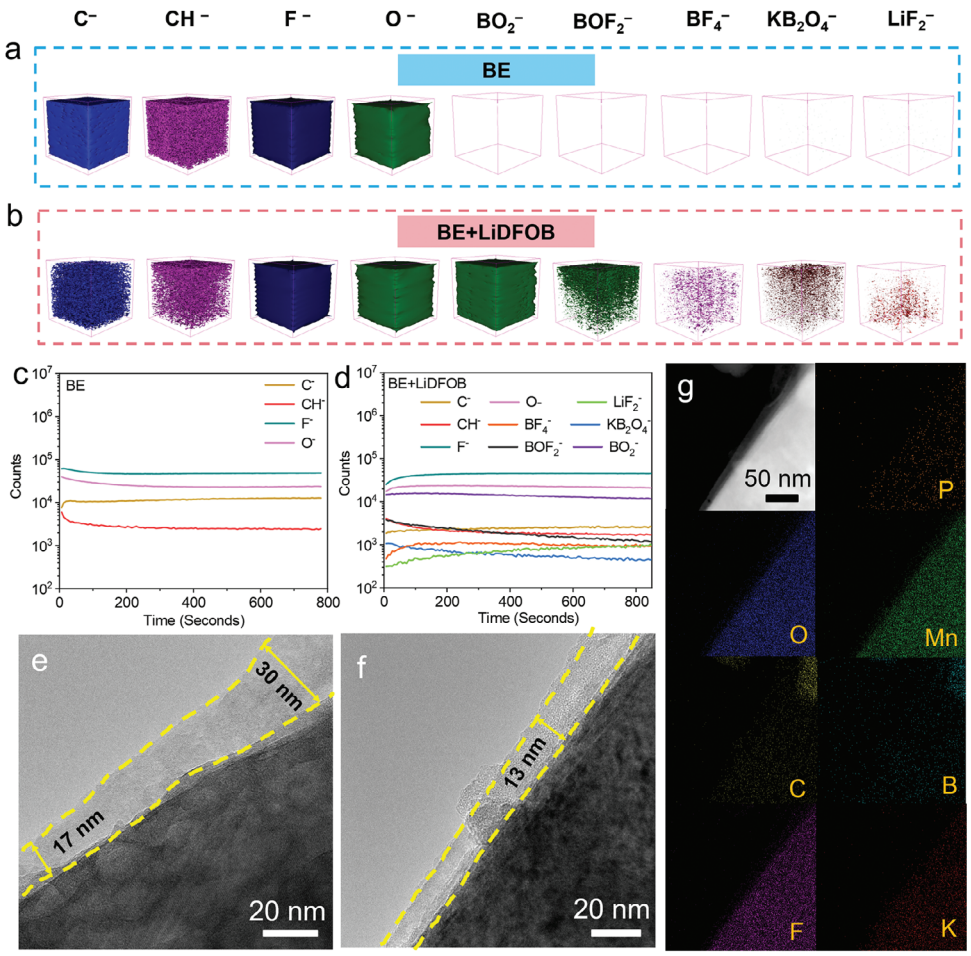

Figure 3. TOF-SIMS 3D reconstructed images of the CEI layer on the KMO surface after 100 cycles in different electrolytes: a) BE and b) BE+LiDFOB. Depth profiles of several representative secondary ion fragments obtained from the KMO surface with different electrolytes: c) BE and d) BE+LiDFOB. HRTEM images of the KMO cathode after 100 cycles with different electrolytes: e) BE and f) BE+LiDFOB. g) Element mapping images of the KMO cathode after 100 cycles with BE+LiDFOB.

mechanical properties of the CEI layer.[57] Additionally, the significant presence of LiF signal was observed in the Li 1s data (Figure 2h). Despite bulk LiF's inherent high resistance to ion conduction, forming an in situ LiF-rich CEI layer did not hinder ion transport kinetics due to its thin profile and proximity to KMO (Figure 1g). Therefore, a CEI containing abundant LiF is an optimal barrier that shields the KMO electrode from the corrosive effects of HF and other free radical groups in the electrolyte, effectively suppressing undesirable side reactions. Moreover, introducing LiDFOB results in a significant presence of Li-B-O (193.4 eV, Figure 2g), further contributing to inhibiting electrolyte decomposition and transition metal dissolution.[40]

TOF-SIMS, a powerful characterization technique known for its ultra-high surface sensitivity and chemical selectivity, was used to investigate the CEI on the KMO surface induced by different electrolytes. Figures 3a and b depict the 3D reconstructed images of the KMO surface exposed to different electrolytes. When cycled in the BE, the KMO surface exhibits C^-, CH^-, F^-, and O^- ions. Upon cycling with LiDFOB, a variety of newly generated ions containing F and B, including BO_2^-, BOF_2^-, BF_4^-, $KB_2O_4^-$, and LiF_2-, emerge, suggesting the participation of LiDFOB in the formation of CEI. With increasing depth, there is a reduction in the contents of CH^-, BOF_2^-, and $KB_2O_4^-$ for the CEI with LiDFOB, indicating the formation of a gradient CEI layer. In addition, the KMO surface with BE+LiDFOB shows lower C^- and CH^- concentrations than with BE. This suggests that the addition of LiDFOB suppresses the decomposition of BE. The C^-, F^-, and O^- contents maintained relatively stable throughout varying depths in both cases, which may be attributed to the influence of Super P and PVDF binder in the electrode. Figures 3c and d depict the depth profiles of characteristic secondary-ion fragments (C^-, CH^-, F^-, O^-, BO_2^-, BOF_2^-, BF_4^-, $KB_2O_4^-$, and LiF_2^-) obtained from KMO electrodes after 100 cycles in both electrolytes. By analyzing the profiles, we gain valuable insights into the spatial distribution of the fragments and their potential impact on electrode performance. The consistency between the depth profiles and 3D reconstructed images supports our findings, which are consistent with what has been observed in XPS spectra.

Besides XPS and TOF-SIMS, HETEM was employed to observe the CEI layer directly. HRTEM images of KMO cathodes cycled with/without LiDFOB after 100 cycles are presented in Figures 3e and f. Notably, the KMO cathode cycled without

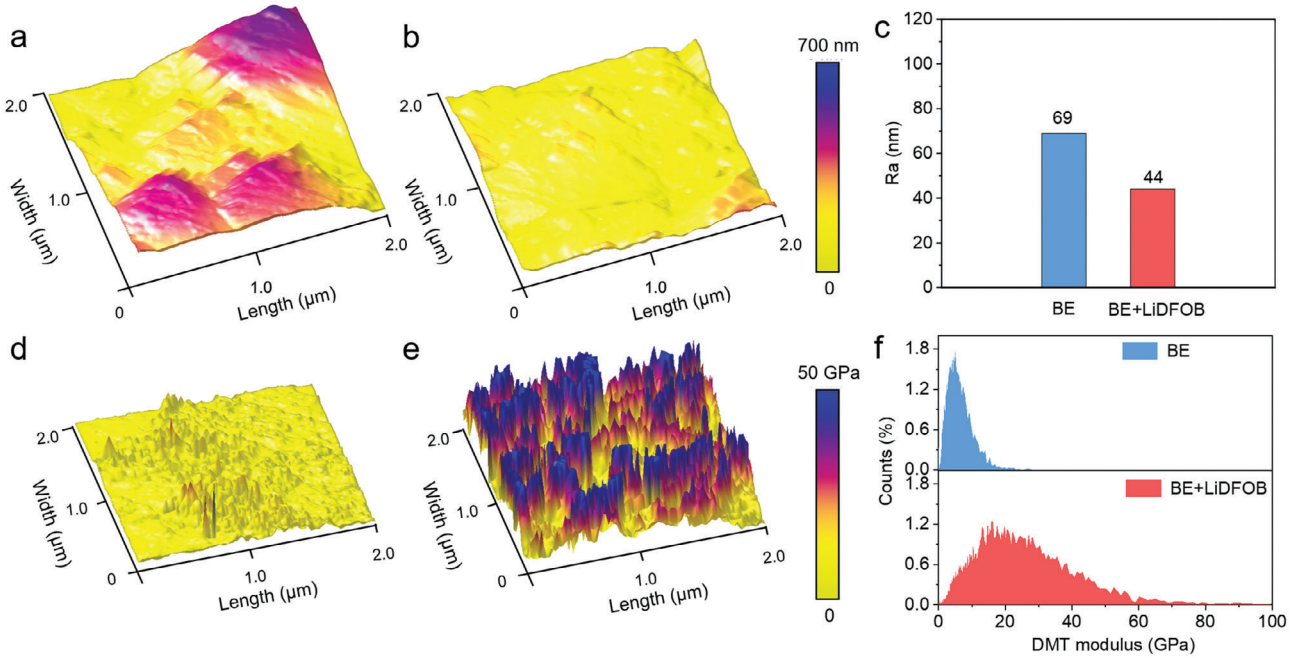

Figure 4. AFM images of KMO surface cycled in a) BE and b) BE+LiDFOB electrolytes. c) Corresponding Ra summarized from AFM results. 3D AFM images of surface modulus distribution for KMO surface cycled in d) BE and e) BE+LiDFOB electrolytes. f) Corresponding DMT modulus summarized from AFM results.

LiDFOB exhibits a non-uniform and thick CEI layer ranging from 17 to 30 nm. In comparison, a uniform and thin CEI layer measuring 13 nm is obtained on the cycled KMO cathode with LiDFOB. This compelling evidence highlights the indispensable role of LiDFOB additive in facilitating the formation of high-quality CEI, which effectively mitigates undesired reactions between cathode material and electrolyte. The thin CEI layer is believed to promote charge transfer and enhance reaction kinetics, as evidenced by EIS spectra. The energy dispersive spectroscopy (EDS) element mapping images of the cycled KMO with BE+LiDFOB in Figure 3g demonstrate a homogeneous distribution of P, O, Mn, C, B, F, and K elements. The XPS, TOF-SIMS, and HETEM results above strongly confirm that the CEI layer formed by the LiDFOB additive is uniform, thin, and rich in B and F species.

To assess the interfacial morphology and mechanical strength of the CEI layer in both BE and BE+LiDFOB electrolytes, atomic force microscopy (AFM) measurements were taken. The measurements were conducted on a KMO electrode disassembled after 100 cycles. The 3D AFM image of the CEI layer on the KMO electrode with the basic electrolyte, shown in **Figure** 4a, displays a fluctuating morphology and a rough interface with an average roughness (Ra) of 69 nm. This suggests an uneven and thick interface caused by severe electrolyte decomposition. Conversely, Figure 4b shows a uniform CEI layer on the KMO electrode with LiDFOB in the basic electrolyte, with a consistently smooth surface and a Ra of 44 nm. This demonstrates the excellent interfacial compatibility and electrochemical stability of the CEI layer.[58] The CEI's mechanical strength was assessed through AFM measurements of the Derjaguin–Müller–Toporov (DMT) modulus. The 3D AFM images in Figures 4d and e show the distribution of surface modulus for the KMO surface cycled in BE and BE+LiDFOB electrolytes. The CEI structure with BE+LiDFOB electrolyte demonstrated a much-enhanced modulus. Figure 4f displays the CEI's average and maximum DMT modulus with BE+LiDFOB at approximately 35.8 and 60 GPa, respectively. These values are three times higher than the corresponding values for the CEI with BE (average: ≈12.4 GPa; maximum: ≈20 GPa).[59,60] In conclusion, adding LiDFOB to the CEI layer improved morphology and mechanical properties.

To gain insights into the oxidative stability of BE and BE+LiDFOB electrolytes, we performed linear scan voltammetry (LSV) measurements on K/stainless steel with the two electrolytes using a scan rate of 0.1 mV s^{-1}. As stated in **Figure** 5a, the addition of LiDFOB induces a new small peak at 3.6 V (vs. K^+/K), probably due to the decomposition of LiDFOB. Figure 5a demonstrates the superior stability of LiDFOB-containing electrolytes up to 5.5 V, in contrast to the basic electrolyte, which undergoes decomposition at ≈4.0 V. This finding suggests that the addition of LiDFOB enhances the oxidation stability of the electrolyte. Density functional theory (DFT) simulations were employed to gain a deeper understanding of the process to calculate the highest occupied molecular orbital (HOMO) energies of KPF_6, LiDFOB, EC, and DEC molecules. Figure 5b illustrates the descending order of HOMO energies for these molecules: LiDFOB (−7.85 eV) > DEC (−8.05 eV) > EC (−8.49 eV) > KPF_6 (−10.72 eV). The higher HOMO energy level of LiDFOB compared to EC, DEC, and KPF_6 suggests that LiDFOB is preferentially involved in the cathodic process, leading to its decomposition and subsequent formation of the F- and B-rich CEI layer. This finding validates the proposed mechanism for CEI formation.

The impact of the F- and B-rich CEI layer on suppressing Mn dissolution in the electrolyte was investigated via ICP-OES. As shown in Figure 5c, the separator subjected to 100 cycles in

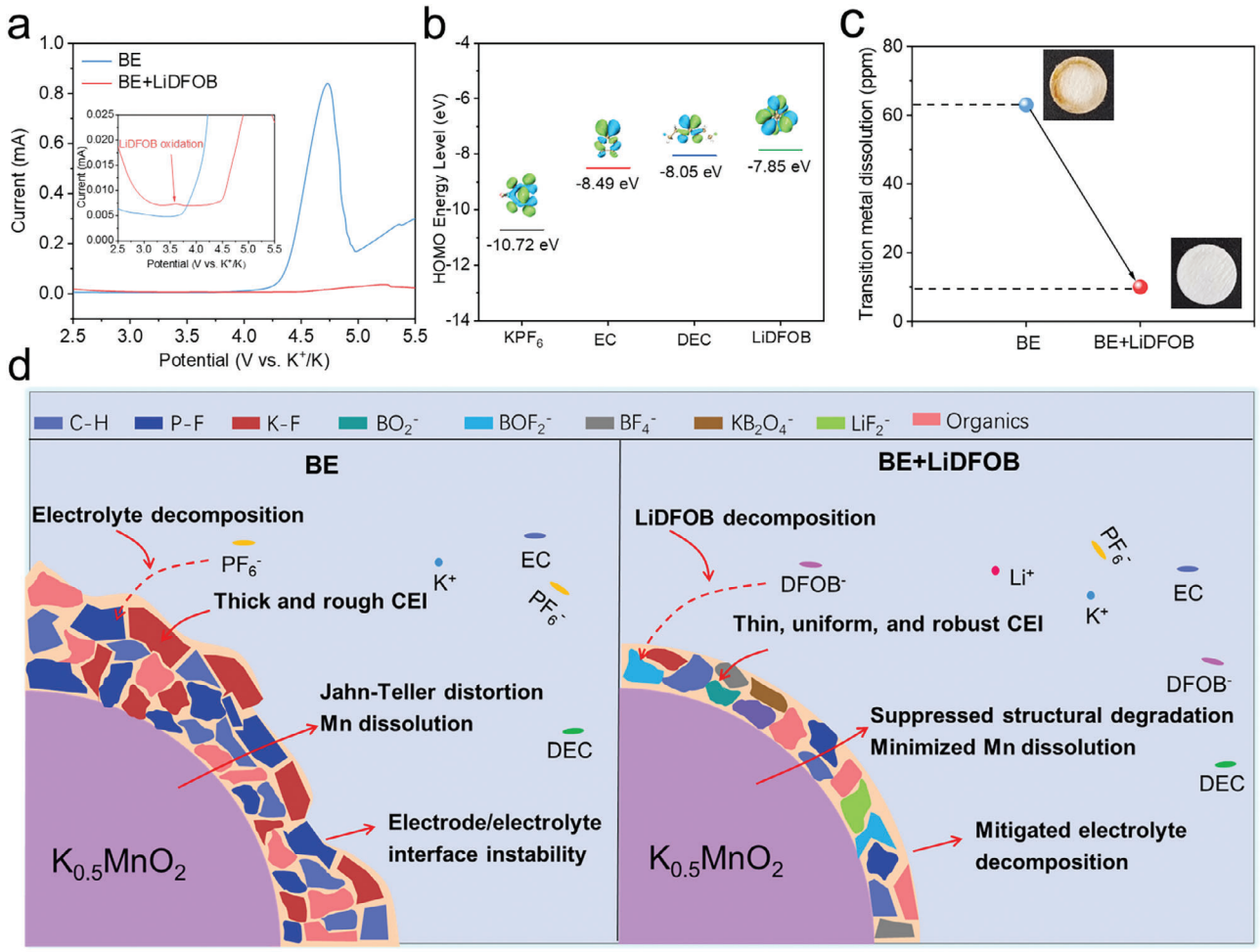

Figure 5. a) Linear scan voltammetry curves of K/stainless steel in different electrolytes at a scan rate of 0.1 mV s^{-1}. b) Calculated HOMOs of KPF_6, LiDFOB, EC, and DEC. c) ICP-OES results for the Mn element content collected from the separators after 100 cycles in BE and BE+LiDFOB. The insert is the corresponding separator. d) Schematic representation showing the issues caused by basic electrolytes and the unique functions of LiDFOB additive.

BE+LiDFOB exhibited a lower Mn content (10 ppm) than that in BE (63 ppm). The inset of Figure 5c demonstrates that the separator remained unchanged without any color variation after undergoing 100 cycles. In contrast, after repeated cycles, the separator with BE exhibits a yellowish hue. These findings highlight the significant impact of F- and B-rich CEI in mitigating electrolyte decomposition and Mn dissolution. Figure 5d comprehensively illustrates the LiDFOB additive's role in enhancing the electrochemical performance of the KMO cathode. In the basic electrolyte, EC molecules can be easily oxidized under the catalysis of O^- (which is produced from the oxidation of lattice oxygen), resulting in the formation of CH_3COO^- and H^+ ions.[61] This will cause severe side reactions between the electrode and electrolyte, resulting in a thick and rough CEI layer composed primarily of C-H, P-F, K-F, and other organic components. This layer fails to effectively suppress Jahn-Teller distortion, Mn dissolution, and side reactions between electrode and electrolyte, resulting in severe structural degradation, poor Coulombic efficiency, and sluggish reaction kinetics. With the introduction of LiDFOB, the intermediates generated by its preferential oxidative decomposition can capture the harmful O^-, H^+, and F^-, forming a thin, uniform, and robust CEI layer enriched with F and B species. These CEI layer components have high antioxidant stability and electronic insulation, which can effectively suppress the decomposition of electrolytes and the subsequent attack of HF to the KMO crystal, thus significantly mitigating structural degradation and Mn dissolution of the cathode.[61] It also improves coulombic efficiency, electron/ion transport kinetics, and cycling durability.[40]

Based on the promising results obtained from the metallic potassium cell experiment discussed earlier, we proceeded to construct a full cell comprising the KMO cathode and soft carbon (SC) anode using the BE+LiDFOB electrolyte and BE electrolyte (as illustrated in **Figure 6a**). The SC anode exhibited impressive electrochemical properties, such as high discharge capacity and exceptional cyclability in the potassium half-cell (Figure S14, supporting information). Charge/discharge curves of KMO||SC, a full cell with BE+LiDFOB electrolyte, were typical and demonstrated in Figure 6b. Specifically, KMO||SC with BE+LiDFOB electrolyte displayed a high CE of above 99%, a reversible specific capacity of 80.8 mAh g^{-1}, and a capacity retention of 71.4% over 20 cycles (Figure 6c). In contrast, KMO||SC with the BE electrolyte showed a lower specific capacity of 51.6 mAh g^{-1} in the

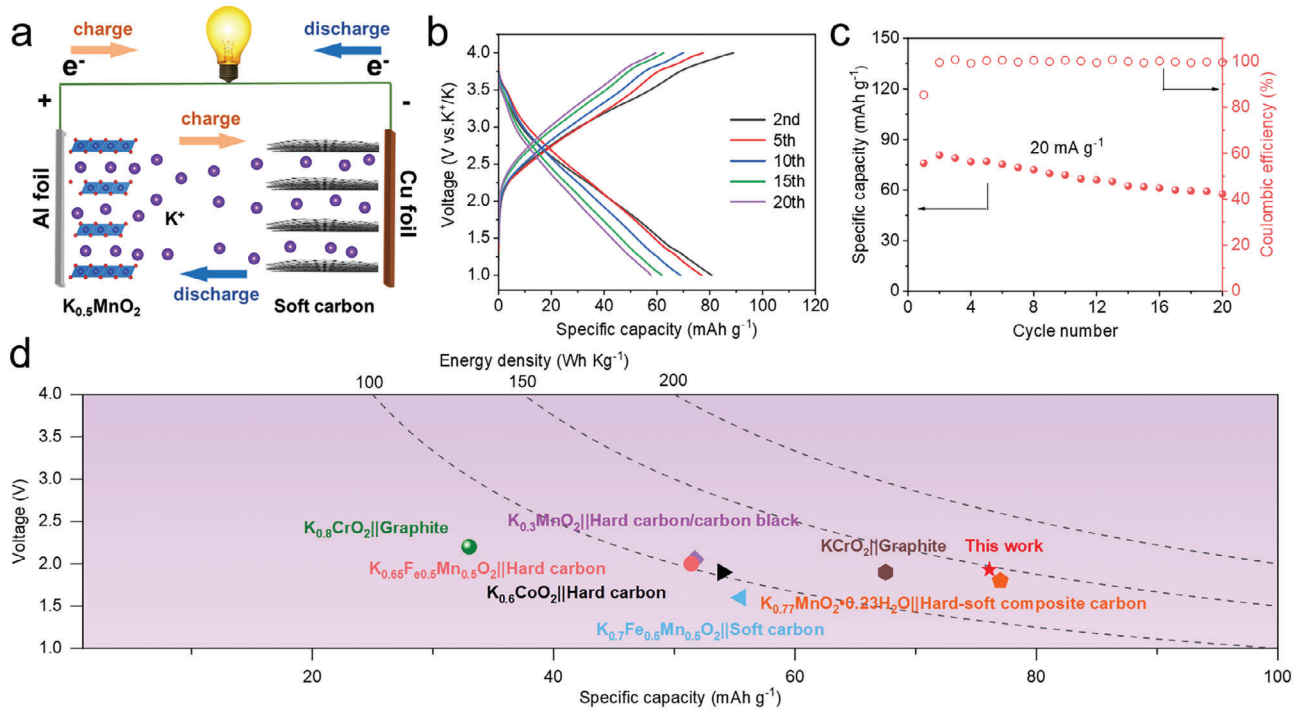

Figure 6. a) Schematic illustration of the K-ion full cell. b) Charge/discharge profiles of KMO||SC full cell in BE+LiDFOB at different cycles between 1.0 and 4.0 V at a current density of 20 mA g^{-1}. c) Cycling performance of KMO||SC full cell in BE+LiDFOB at 20 mA g^{-1} in a 1.0–4.0 V voltage range. d) Average discharge voltage and energy density versus capacity of some reported K-ion full-cells. Note: both the capacity and energy density of the KMO||SC full cell are calculated based on the total mass of the cathode and anode materials, and the data used for plotting Figure 6d are listed in Table S2 (Supporting Information).

first cycle, and the CE is always below 80% for the first ten cycles, indicating severe electrolyte decomposition (Figure S15, Supporting Information). Based on the total weight of the cathode and anode materials, the KMO||SC full cell reaches an energy density of 167.3 Wh kg^{-1} (Figure 6d and Table S2, Supporting Information). This is one of the highest recorded energy densities for K-ion full-cell with layered oxide cathodes.[18,44,62–65]

3. Conclusion

To summarize, we have discovered LiDFOB as a new electrolyte additive for PIBs and studied its origin in enhancing the electrochemical stability and kinetics of the KMO cathode. Our findings show that LiDFOB breaks down before KPF_6, EC, and DEC during the cathodic process, acting as an oxidative sacrificial agent that improves the physicochemical properties of the CEI layer on the KMO cathode. The CEI layer, which has appropriate chemical compositions rich in F and B species, dramatically enhances the structural stability of KMO, protects against various side reactions, and reduces Mn loss. The CEI-modified P3-KMO with F- and B-rich composition exhibits a high Coulombic efficiency of ≈99.5% and a capacity retention rate of 78.6% after 300 cycles. The KMO||SC K-ion full cell shows a high reversible capacity of 80.1 mAh g^{-1} at 20 mA g^{-1} and a high energy density of 167.3 Wh kg^{-1}. This study provides valuable insights into the in situ CEI construction on the KMO cathode for enhancing the performance of PIBs, considering the multifunctional electrolyte additive's effectiveness, convenience, and low cost.

4. Experimental Section

Material Synthesis: Synthesis of $MnCO_3$. To start the process, 0.98 g of $Mn(CH_3COO)_2{\cdot}4H_2O$ and 2.37 g of NH_4HCO_3 were mixed with 40 mL of ethylene glycol and stirred for 30 minutes at room temperature. Next, the solution was heated to 200 °C for 20 hours in a 50 mL Teflon-lined stainless steel autoclave. Afterward, $MnCO_3$ was obtained by centrifugation at 4000 rpm for 5 minutes, washed multiple times with deionized water and absolute ethanol, and dried in a vacuum at 60°C overnight.

Synthesis of $K_{0.5}MnO_2$: To synthesize Mn_2O_3, $MnCO_3$ was annealed in the air at 500 °C for four hours. Then, 0.40 g of Mn_2O_3 and 0.19 g of KOH were mixed thoroughly by ball-milling and calcined at 850 °C for ten hours under an air atmosphere, producing $K_{0.5}MnO_2$.

Synthesis of Soft Carbon: The soft carbon anode materials were prepared by thermal pyrolysis of perylene-3,4,9,10-tetracarboxylic dianhydride (PTCDA, Aladdin) at 900 °C for 10 h in flowing Ar gas.

Electrolyte Preparation and Battery Assembly: The basic electrolyte, purchased from DoDoChem, consisted of 0.8 mol L^{-1} KPF_6 dissolved in a mixed solvent of ethylene carbonate and dimethyl carbonate (1:1, v/v). To prepare the LiDFOB-containing electrolyte, LiDFOB salt (≥ 99.9%, DoDoChem) was added to the basic electrolyte.

To create the cathode slurry, a mixture of $K_{0.5}MnO_2$, Super P, and polyvinylidene fluoride binder was combined in a ratio of 7:2:1 by weight. The mixture was then dispersed in 1-methyl-2-pyrrolidinone. Afterward, the slurry was placed onto an Al foil and dried at 80 °C overnight under a vacuum. To form circular discs measuring 12 mm, the dried aluminum foil was pressed with a rolling machine and punched out. The active material on the electrode was around 1.2 mg cm^{-2}. To prepare the soft carbon anode, a slurry containing 70% soft carbon, 20% acetylene black, and 10% carboxymethyl cellulose (CMC) was spread onto the Cu foil. The electrodes were left to dry overnight at 80 °C. The mass loading of soft carbon was around 0.4 mg cm^{-2}. CR2032 coin cells were assembled inside an Ar-filled

glove box (with H_2O content < 0.1 ppm and O_2 content < 0.1 ppm). The K||KMO half-cell consisted of a K sheet as the anode, a $K_{0.5}MnO_2$ electrode as the cathode, and a Whatman GF/D glass microfiber filter as the separator. The KMO||SC full cell used a soft carbon electrode as the anode. Before assembling the full cell, the $K_{0.5}MnO_2$ and soft carbon electrodes were activated in the metallic potassium cell for 8 cycles. Each cell was filled with approximately 80 µL of electrolyte.

Material Characterization: Various methods were used to analyze our samples. X-ray diffraction patterns were collected using a PANalytical X'Pert Pro MPD with Cu-Kα radiation (λ = 1.54178 Å) and diagnosed with the GSAS Rietveld program. Electrochemical impedance spectroscopy (EIS) measurements were conducted on an electrochemical workstation (Gamry-Reference 3000) in the frequency range of 0.01–100 kHz. Our X-ray photoelectron spectroscopy (XPS) and scanning electron microscopy (SEM) results were obtained using a Thermo Fischer ESCALAB 250 X-ray photoelectron spectrometer and a JEOL JSM-7500F field-emission scanning electron microscope. Transmission electron microscopy (TEM) and energy dispersive spectroscopy (EDS) maps were recorded by using an FEI Tecnai G2 F30 field emission transmission electron microscope. Atomic force microscopy (AFM) measurements were conducted via tapping mode on a Brucker Bioscope Resolve scanning probe microscope (Germany). To study element compositions, inductively coupled plasma optical emission spectrometry (ICP-OES, PerkinElmer OPTIMA 8300) was used. For surface analysis, TOF-SIMS analysis was performed using a PHI nanoTOF II time-of-flight SIMS with a 30 kV Bi-cluster liquid metal ion gun (LMIG). The electrodes were fixed with a metallic mask on the sample holder to avoid air exposure and transferred them from the glove box to the spectrometer using a transfer vessel. The same experimental conditions were used for all mass spectra acquisition, allowing semiquantitative analysis. The LMIG gun was set to deliver Bi^{3+} primary ions with a DC of 2 nA, and the number of frames were put to 30 for both positive and negative polarities. For depth profile experiments, a 5 kV Ar^+ gas gun was used with an etching time of 20 s for each cycle and a DC of 300 nA.

Electrochemical measurements: Galvanostatic charge/discharge tests were conducted on a battery testing system (LAND CT-2001A, China) at room temperature, ranging from 1.5 to 4.0 V. To obtain cyclic voltammetry (CV) curves, a CHI 760E electrochemical workstation was used. LSV was also performed using a two-electrode system consisting of a stainless steel sheet as the working electrode and a K sheet as the counter electrode.

Density Function Theory (DFT) Calculations: DFT calculations were performed on the Gaussian 09 software package. The molecular geometrical configurations were optimized at the B3LYP/6-311++G(d) level. The liquid environment simulation was considered using the continuous polarization medium model (PCM) method with the dielectric constant of acetone. Frequency analyses were done at the same level to confirm the obtained optimized stationary point.[66] The 3D images of key species were generated by the Multiwfn program and VMD 1.9.3 program.[67]

Supporting Information

Supporting Information is available from the Wiley Online Library or from the author.

Acknowledgements

F.L. and X.G. contributed equally to this work. The authors would like to express their gratitude for the financial support received from the National Natural Science Foundation of China (22378426, 22138013), the Taishan Scholar Project (ts201712020), the Natural Science Foundation of Shandong Province (ZR2022MB088).

Conflict of interest

The authors declare no conflict of interest.

Data Availability Statement

The data that support the findings of this study are available from the corresponding author upon reasonable request.

Keywords

cathode-electrolyte interphase, electrolyte additive, lithium difluoro(oxalate) borate, manganese-based layered oxide cathode, potassium-ion battery

Received: October 23, 2023
Revised: December 30, 2023
Published online: January 9, 2024

[1] Y.-H. Zhu, X. Yang, T. Sun, S. Wang, Y.-L. Zhao, J.-M. Yan, X.-B. Zhang, *Electrochem. Energy Rev.* **2018**, *1*, 548.
[2] Q. Zhang, Z. Wang, S. Zhang, T. Zhou, J. Mao, Z. Guo, *Electrochem. Energy Rev.* **2018**, *1*, 625.
[3] X. Gu, J. Wang, X. Zhao, X. Jin, Y. Jiang, P. Dai, N. Wang, Z. Bai, M. Zhang, M. Wu, *J. Energy Chem.* **2023**, *85*, 30.
[4] Z. Cheng, L. Guo, Q. Dong, C. Wang, Q. Yao, X. Gu, J. Yang, Y. Qian, *Adv. Energy Mater.* **2022**, *12*, 2202253.
[5] K. V. Kravchyk, P. Bhauriyal, L. Piveteau, C. P. Guntlin, B. Pathak, M. V. Kovalenko, *Nat. Commun.* **2018**, *9*, 4469.
[6] J. Xiao, F. Shi, T. Glossmann, C. Burnett, Z. Liu, *Nat. Energy* **2023**, *8*, 329.
[7] S. Xia, X. Wu, Z. Zhang, Y. Cui, W. Liu, *Chem* **2019**, *5*, 753.
[8] Y.-S. Xu, S.-J. Guo, X.-S. Tao, Y.-G. Sun, J. Ma, C. Liu, A.-M. Cao, *Adv. Mater.* **2021**, *33*, 2100409.
[9] X. Min, J. Xiao, M. Fang, W. (A.). Wang, Y. Zhao, Y. Liu, A. M. Abdelkader, K. Xi, R. V Kumar, Z. Huang, *Energy Environ. Sci.* **2021**, *14*, 2186.
[10] S. Wen, X. Gu, X. Ding, P. Dai, D. Zhang, L. Li, D. Liu, X. Zhao, J. Yang, *Adv. Funct. Mater.* **2022**, *32*, 2106751.
[11] L. Deng, J. Qu, X. Niu, J. Liu, J. Zhang, Y. Hong, M. Feng, J. Wang, M. Hu, L. Zeng, Q. Zhang, L. Guo, Y. Zhu, *Nat. Commun.* **2021**, *12*, 2167.
[12] A. Zhou, W. Cheng, W. Wang, Q. Zhao, J. Xie, W. Zhang, H. Gao, L. Xue, J. Li, *Adv. Energy Mater.* **2021**, *11*, 2000943.
[13] K.-Y. Zhang, Z.-Y. Gu, E. H. Ang, J.-Z. Guo, X.-T. Wang, Y. Wang, X.-L. Wu, *Mater. Today* **2022**, *54*, 189.
[14] X. Zhang, Y. Yang, X. Qu, Z. Wei, G. Sun, K. Zheng, H. Yu, F. Du, *Adv. Funct. Mater.* **2019**, *29*, 1905679.
[15] M. G. T. Nathan, H. Yu, G.-T. Kim, J.-H. Kim, J. S. Cho, J. Kim, J.-K. Kim, *Adv. Sci.* **2022**, *9*, 2105882.
[16] J. U. Choi, J. Kim, J.-Y. Hwang, J. H. Jo, Y.-K. Sun, S.-T. Myung, *Nano Energy* **2019**, *61*, 284.
[17] Y.-S. Xu, S.-J. Guo, X.-S. Tao, Y.-G. Sun, J. Ma, C. Liu, A.-M. Cao, *Adv. Mater.* **2021**, *33*, 2100409.
[18] X. Wang, X. Xu, C. Niu, J. Meng, M. Huang, X. Liu, Z. Liu, L. Mai, *Nano Lett.* **2017**, *17*, 544.
[19] X. Wang, P. Hu, C. Niu, J. Meng, X. Xu, X. Wei, C. Tang, W. Luo, L. Zhou, Q. An, L. Mai, *Nano Energy* **2017**, *35*, 71.
[20] J.-Y. Hwang, J. Kim, T.-Y. Yu, H.-G. Jung, J. Kim, K-H. Kim, Y.-K. Sun, *J. Mater. Chem. A* **2019**, *7*, 21362.
[21] C.-l. Liu, S.-h. Luo, H.-b. Huang, X. Liu, Y.-c. Zhai, Z.-w. Wang, *Chem. Eng. J.* **2019**, *378*, 122167.
[22] X. Zhang, D. Yu, Z. Wei, N. Chen, G. Chen, Z. X. Shen, F. Du, *ACS Appl. Mater. Interfaces* **2021**, *13*, 18897.
[23] Z. Xiao, J. Meng, F. Xia, J. Wu, F. Liu, X. Zhang, L. Xu, X. Lin, L. Mai, *Energy Environ. Sci.* **2020**, *13*, 3129.

[24] B. Peng, Y. Li, J. Gao, F. Zhang, J. Li, G. Zhang, *J. Power Sources* **2019**, *437*, 226913.
[25] M. G. T. Nathan, N. Naveen, W. B. Park, K.-S. Sohn, M. Pyo, *J. Power Sources* **2019**, 438, 226992.
[26] C.-L. Liu, S.-H. Luo, H.-B. Huang, Y.-C. Zhai, Z.-W. Wang, *Chem. Eng. J.* **2019**, *356*, 53.
[27] C.-L. Liu, S.-H. Luo, H.-B. Huang, Y.-C. Zhai, Z.-W. Wang, *ChemElectroChem* **2019**, *6*, 2308.
[28] R. Huang, Q. Xue, J. Lin, X. Zhang, J. Zhou, F. Wu, L. Li, R. Chen, *Nano Res.* **2021**, *15*, 3143.
[29] J. Weng, J. Duan, C. Sun, P. Liu, A. Li, P. Zhou, J. Zhou, *Chem. Eng. J.* **2020**, *392*, 123649.
[30] P. Bai, K. Jiang, X. Zhang, J. Xu, S. Guo, H. Zhou, *ACS Appl. Mater. Interfaces* **2020**, *12*, 10490.
[31] Z. Zhang, J. Sun, L. Duan, Y. Du, J. Li, J. Shen, X. Zhou, *J. Mater. Chem. A* **2022**, *10*, 554.
[32] J. U. Choi, J. Kim, J. H. Jo, H. J. Kim, Y. H. Jung, D.-C. Ahn, Y.-K. Sun, S.-T. Myung, *Energy Stor. Mater.* **2020**, *25*, 714.
[33] L. Liu, J. Liang, W. Wang, C. Han, Q. Xia, X. Ke, J. Liu, Q. Gu, Z. Shi, S. Chou, S. Dou, W. Li, *ACS Appl. Mater. Interfaces* **2021**, *13*, 28369.
[34] Q. Zhang, C. Didier, W. K. Pang, Y. Liu, Z. Wang, S. Li, V. K. Peterson, J. Mao, Z. Guo, *Adv. Energy Mater.* **2019**, *9*, 1900568.
[35] R.-J. Luo, X.-L. Li, J.-Y. Ding, J. Bao, C. Ma, C.-Y. Du, X.-Y. Cai, X.-J. Wu, Y.-N. Zhou, *Energy Stor. Mater.* **2022**, *47*, 408.
[36] Y. Huang, X. Zhang, N. Chen, R. Tian, Y. Zeng, F. Du, *Small* **2023**, *19*, 2302841.
[37] L. Deng, T. Wang, Y. Hong, M. Feng, R. Wang, J. Zhang, Q. Zhang, J. Wang, L. Zeng, Y. Zhu, L. Guo, *ACS Energy Lett.* **2020**, *5*, 1916.
[38] K. Lei, Z. Zhu, Z. Yin, P. Yan, F. Li, J. Chen, *Chem* **2019**, *5*, 3220.
[39] L. Chen, X. Fan, E. Hu, X. Ji, J. Chen, S. Hou, T. Deng, J. Li, D. Su, X. Yang, C. Wang, *Chem* **2019**, *5*, 896.
[40] T. Deng, X. Fan, L. Cao, J. Chen, S. Hou, X. Ji, L. Chen, S. Li, X. Zhou, E. Hu, D. Su, X.-Q. Yang, C. Wang, *Joule* **2019**, *3*, 2550.
[41] F. Cheng, X. Zhang, P. Wei, S. Sun, Y. Xu, Q. Li, C. Fang, J. Han, Y. Huang, *Sci. Bull.* **2022**, *67*, 2225.
[42] X. Ou, G. Zhang, S. Zhang, X. Tong, Y. Tang, *Energy Stor. Mater.* **2020**, *28*, 357.
[43] J. Liang, C. Lin, X. Meng, M. Liang, J. Lai, X. Zheng, Q. Huang, L. Liu, Z. Shi, *J. Mater. Chem. A* **2021**, *9*, 17261.
[44] T. Deng, X. Fan, J. Chen, L. Chen, C. Luo, X. Zhou, J. Yang, S. Zheng, C. Wang, *Adv. Funct. Mater.* **2018**, *28*, 1800219
[45] R. Weber, M. Genovese, A. J. Louli, S. Hames, C. Martin, I. G. Hill, J. R. Dahn, *Nat. Energy* **2019**, *4*, 683.
[46] X. Min, C. Han, S. Zhang, J. Ma, N. Hu, J. Li, X. Du, B. Xie, H.-J. Lin, C.-Y. Kuo, C.-T. Chen, Z. Hu, L. Qiao, Z. Cui, G. Xu, G. Cui, *Angew. Chem., Int. Ed.* **2023**, *62*, e202302664.
[47] M. Li, H. An, Y. Song, Q. Liu, J. Wang, H. Huo, S. Lou, J. Wang, *J. Am. Chem. Soc.* **2023**, *145*, 25632.
[48] D. Zhang, Y. Liu, Z. Sun, Z. Liu, X. Xu, L. Xi, S. Ji, M. Zhu, J. Liu, *Angew. Chem., Int. Ed.* **2023**, *62*, e202310006.
[49] S. Zhao, Z. Liu, G. Xie, Z. Guo, S. Wang, J. Zhou, X. Xie, B. Sun, S. Guo, G. Wang, *Energy Environ. Sci.* **2022**, *15*, 3015.
[50] Y.-S. Xu, Y.-N. Zhou, Q.-H. Zhang, M.-Y. Qi, S.-J. Guo, J.-M. Luo, Y.-G. Sun, L. Gu, A.-M. Cao, L.-J. Wan, *Chem. Eng. J.* **2021**, *412*, 128735.
[51] C.-L. Liu, S.-H. Luo, H.-B. Huang, Y.-C. Zhai, Z.-W. Wang, *Electrochim. Acta* **2018**, *286*, 114.
[52] R. Dang, N. Li, Y. Yang, K. Wu, Q. Li, Y. L. Lee, X. Liu, Z. Hu, X. Xiao, *J. Power Sources* **2020**, *464*, 228190.
[53] S. Park, S. Park, Y. Park, M. H. Alfaruqi, J.-Y. Hwang, J. Kim, *Energy Environ. Sci.* **2021**, *14*, 5864.
[54] Q. Deng, F. Zheng, W. Zhong, Q. Pan, Y. Liu, Y. Li, G. Chen, Y. Li, C. Yang, M. Liu, *Chem. Eng. J.* **2020**, 392,
[55] Y. Wang, Y. Zhang, S. Wang, S. Dong, C. Dang, W. Hu, D. Y. W. Yu, *Adv. Funct. Mater.* **2021**, *31*, 2102360.
[56] F. Cheng, X. Zhang, Y. Qiu, J. Zhang, Y. Liu, P. Wei, M. Ou, S. Sun, Y. Xu, Q. Li, C. Fang, J. Han, Y. Huang, *Nano Energy* **2021**, *88*, 106301.
[57] C. Wu, J. Hu, Q. Yang, M. Lei, Y. Yu, C. Lai, C. Li, *Nano Energy* **2023**, *113*, 108523.
[58] J. Liu, Y. Zhang, H. Ji, J. Zhang, P. Zhou, Y. Cao, J. Zhou, C. Yan, T. Qian, *Adv. Sci.* **2022**, *9*, e2200390.
[59] Q.-K. Zhang, X.-Q. Zhang, J. Wan, N. Yao, T.-L. Song, J. Xie, L.-P. Hou, M.-Y. Zhou, X. Chen, B.-Q. Li, R. Wen, H.-J. Peng, Q. Zhang, J.-Q. Huang, *Nat. Energy* **2023**, *8*, 725.
[60] Y. Yan, S. Weng, A. Fu, H. Zhang, J. Chen, Q. Zheng, B. Zhang, S. Zhou, H. Yan, C.-W. Wang, Y. Tang, H. Luo, B.-W. Mao, J. Zheng, X. Wang, Y. Qiao, Y. Yang, S.-G. Sun, *ACS Energy Lett.* **2022**, *7*, 2677.
[61] L. Yang, J. Chen, S. Park, H. Wang, *Energy Mater.* **2023**, *3*, 3000029.
[62] C. Vaalma, G. A. Giffin, D. Buchholz, S. Passerini, *J. Electrochem. Soc.* **2016**, *163*, A1295.
[63] T. Deng, X. Fan, C. Luo, J. Chen, L. Chen, S. Hou, N. Eidson, X. Zhou, C. Wang, *Nano Lett.* **2018**, *18*, 1522.
[64] B. Lin, X. Zhu, L. Fang, X. Liu, S. Li, T. Zhai, L. Xue, Q. Guo, J. Xu, H. Xia, *Adv. Mater.* **2019**, *31*, 1900060.
[65] N. Naveen, S. C. Han, S. P. Singh, D. Ahn, K.-S. Sohn, M. Pyo, *J. Power Sources* **2019**, *430*, 137.
[66] J. Chen, Y. Peng, Y. Yin, M. Liu, Z. Fang, Y. Xie, B. Chen, Y. Cao, L. Xing, J. Huang, Y. Wang, X. Dong, Y. Xia, *Energy Environ. Sci.* **2022**, *15*, 3360.
[67] T. Lu, F. Chen, *J. Comput. Chem.* **2012**, *33*, 580.